

Yields and production rates of ${}^9\text{Li}$ and ${}^8\text{He}$ measured with the Double Chooz near and far detectors



The Double Chooz Collaboration

H. de Kerret,^d T. Abrahão,^e H. Almazan,^o J.C. dos Anjos,^e S. Appel,^v J.C. Barriere,^k I. Bekman,^a T.J.C. Bezerra,^r L. Bezrukov,^j E. Blucher,^g T. Brugière,^q C. Buck,^o J. Busenitz,^b A. Cabrera,^{d,aa} M. Cerrada,^h E. Chauveau,^f P. Chimenti,^{e,2} O. Corpace,^k J.V. Dawson,^d Z. Djurcic,^c A. Etenko,ⁿ D. Franco,^d H. Furuta,^s I. Gil-Botella,^h A. Givaudan,^d H. Gomez,^d L.F.G. Gonzalez,^y M.C. Goodman,^c T. Hara,^m J. Haser,^o D. Hellwig,^a A. Hourlier,^{d,3} M. Ishitsuka,^{t,4} J. Jochum,^w C. Jollet,^f K. Kale,^{f,q} M. Kaneda,^t M. Karakac,^d T. Kawasaki,^l E. Kemp,^y D. Kryn,^d M. Kuze,^t T. Lachenmaier,^w C.E. Lane,ⁱ T. Lasserre,^{k,d} C. Lastoria,^h D. Lhuillier,^k H.P. Lima Jr,^e M. Lindner,^o J.M. López-Castaño,^h J.M. LoSecco,^p B. Lubsandorzhev,^j J. Maeda,^{u,m} C. Mariani,^z J. Maricic,^{i,5} J. Martino,^r T. Matsubara,^{u,6} G. Mention,^k A. Mereaglia,^f T. Miletic,^{i,7} R. Milincic,^{i,5} D. Navas-Nicolás,^h P. Novella,^{h,8} H. Nunokawa,^{e,9} L. Oberauer,^v M. Obolensky,^d A. Onillon,^d A. Oralbaev,ⁿ C. Palomares,^h I.M. Pepe,^e G. Pronost,^{r,10} J. Reichenbacher,^{b,11} B. Reinhold,^{o,5} M. Settimo,^r S. Schönert,^v S. Schoppmann,^o L. Scola,^k R. Sharankova,^t V. Sibille,^{k,1,3} V. Sinev,^j M. Skorokhvatov,ⁿ P. Soldin,^a A. Stahl,^a I. Stancu,^b L.F.F. Stokes,^{w,1,12} F. Suekane,^{s,d} S. Sukhotin,ⁿ T. Sumiyoshi,^u Y. Sun,^{b,5} A. Tonazzo,^d C. Veysièrè,^k B. Viaud,^r M. Vivier,^k S. Wagner,^{d,e} C. Wiebusch,^a M. Wurm,^{w,13} G. Yang,^{c,14} F. Yermia^r

¹Corresponding author

²Now at Universidade Estadual de Londrina, 86057-970 Londrina, Brazil

³Now at Massachusetts Institute of Technology, Cambridge, Massachusetts 02139, USA

⁴Now at Tokyo University of Science, Noda, Chiba, Japan

⁵Now at Physics & Astronomy Department, University of Hawaii at Manoa, Honolulu, Hawaii, USA

⁶Now at High Energy Accelerator Research Organization (KEK), Tsukuba, Ibaraki, Japan

⁷Now at Physics Department, Arcadia University, Glenside, PA 19038

⁸Now at Instituto de Física Corpuscular, IFIC (CSIC/UV), 46980 Paterna, Spain

⁹Now at Pontifícia Universidade Católica do Rio de Janeiro, Rio de Janeiro, Brazil

¹⁰Now at Kamioka Observatory, Institute for Cosmic Ray Research, University of Tokyo, Kamioka, Japan

¹¹Now at South Dakota School of Mines & Technology, Rapid City, SD 57701

¹²Now at INFN Laboratori Nazionali del Gran Sasso, 67100 Assergi (AQ), Italy

¹³Now at Institut für Physik and Excellence Cluster PRISMA, Johannes Gutenberg-Universität Mainz, 55128 Mainz, Germany

¹⁴Now at State University of New York at Stony Brook, Stony Brook, NY, 11755, USA

- ^aIII. Physikalisches Institut, RWTH Aachen University, 52056 Aachen, Germany
- ^bDepartment of Physics and Astronomy, University of Alabama, Tuscaloosa, Alabama 35487, USA
- ^cArgonne National Laboratory, Argonne, Illinois 60439, USA
- ^dAstroParticule et Cosmologie, CNRS/IN2P3, CEA/IRFU, Observatoire de Paris, Sorbonne Paris Cité, 75205 Paris Cedex 13, France
- ^eCentro Brasileiro de Pesquisas Físicas, Rio de Janeiro, RJ, 22290-180, Brazil
- ^fUniversité de Bordeaux, CNRS/IN2P3, CENBG, F-33175 Gradignan, France
- ^gThe Enrico Fermi Institute, The University of Chicago, Chicago, Illinois 60637, USA
- ^hCentro de Investigaciones Energéticas, Medioambientales y Tecnológicas, CIEMAT, 28040, Madrid, Spain
- ⁱDepartment of Physics, Drexel University, Philadelphia, Pennsylvania 19104, USA
- ^jInstitute of Nuclear Research of the Russian Academy of Sciences, Moscow 117312, Russia
- ^kCommissariat à l’Energie Atomique et aux Energies Alternatives, Centre de Saclay, IRFU, 91191 Gif-sur-Yvette, France
- ^lDepartment of Physics, Kitasato University, Sagami-hara, 252-0373, Japan
- ^mDepartment of Physics, Kobe University, Kobe, 657-8501, Japan
- ⁿNRC Kurchatov Institute, 123182 Moscow, Russia
- ^oMax-Planck-Institut für Kernphysik, 69117 Heidelberg, Germany
- ^pUniversity of Notre Dame, Notre Dame, Indiana 46556, USA
- ^qIPHC, CNRS/IN2P3, Université de Strasbourg, 67037 Strasbourg, France
- ^rSUBATECH, CNRS/IN2P3, Université de Nantes, IMT-Atlantique, 44307 Nantes, France
- ^sResearch Center for Neutrino Science, Tohoku University, Sendai 980-8578, Japan
- ^tDepartment of Physics, Tokyo Institute of Technology, Tokyo, 152-8551, Japan
- ^uDepartment of Physics, Tokyo Metropolitan University, Tokyo, 192-0397, Japan
- ^vPhysik Department, Technische Universität München, 85748 Garching, Germany
- ^wKepler Center for Astro and Particle Physics, Universität Tübingen, 72076 Tübingen, Germany
- ^yUniversidade Estadual de Campinas-UNICAMP, Campinas, SP, 13083-970, Brazil
- ^zCenter for Neutrino Physics, Virginia Tech, Blacksburg, Virginia 24061, USA
- ^{aa}LNCA Underground Laboratory, IN2P3/CNRS - CEA, Chooz, France

E-mail: lee.stokes@lngs.infn.it, vsibille@mit.edu, anatael@in2p3.fr

ABSTRACT: The yields and production rates of the radioisotopes ${}^9\text{Li}$ and ${}^8\text{He}$ created by cosmic muon spallation on ${}^{12}\text{C}$ have been measured by the Double Chooz experiment. Comparing the data to a detailed simulation of the ${}^9\text{Li}$ and ${}^8\text{He}$ decays, the contribution of the ${}^8\text{He}$ radioisotope is found to be compatible with zero. The observed ${}^9\text{Li}$ yields in the near (~ 120 m.w.e overburden) and far (~ 300 m.w.e.) detectors are 4.37 ± 0.49 and 7.98 ± 0.52 respectively, in units of $10^{-8} \mu^{-1} \text{g}^{-1} \text{cm}^2$. The low overburdens of the near and far detectors gives a unique insight when combined with measurements by KamLAND and Borexino to give the first multi-experiment, data driven relationship between the ${}^9\text{Li}$ yield and the mean muon energy according to the power law $Y = Y_0 \langle E_\mu \rangle^{\bar{\alpha}}$, giving $\bar{\alpha} = 0.79 \pm 0.06$ and $Y_0 = (0.29 \pm 0.09) \times 10^{-8} \mu^{-1} \text{g}^{-1} \text{cm}^2$. This relationship gives future liquid scintillator based nuclear reactor experiments the ability to predict their cosmogenic ${}^9\text{Li}$ background rates.

KEYWORDS: neutrino detectors, neutrino experiments

Contents

1	Introduction	1
2	The Double Chooz detectors	2
3	Cosmogenic spectra prediction	3
3.1	Raw spectra generation	3
3.2	Mean spectrum and covariance building	4
3.3	Resulting ${}^9\text{Li}$ and ${}^8\text{He}$ spectra	5
4	Measurements	5
4.1	Selection of ${}^9\text{Li}$ and ${}^8\text{He}$ Candidates	6
4.2	${}^8\text{He}$ Fraction Measurements	7
4.3	Cosmogenic yields, production rates and cross sections	8
5	Conclusion	11

1 Introduction

The Double Chooz experiment (DC) provided a measurement of the neutrino mixing angle θ_{13} , firstly using the far detector only [1, 2] and recently with two detectors [3] which allows most of the systematics to cancel each other out, in particular from the neutrino flux. Anti-neutrino detection is based on the Inverse Beta Decay (IBD) process ($\bar{\nu}_e + p \rightarrow e^+ + n$) in liquid scintillators, where the neutron is predominantly captured on Hydrogen (H) or Gadolinium (Gd) corresponding to released energies of 2.2 MeV and ~ 8 MeV respectively. This interaction is identified by a fast coincidence signal, consisting of the prompt positron signal and then the delayed n -capture.

Cosmic muons interact with ${}^{12}\text{C}$ present in the liquid scintillator creating radioisotopes through muon spallation processes. Their formation by muon capture has already been measured by DC [4]. Of the cosmogenic radioisotopes, ${}^9\text{Li}$ and ${}^8\text{He}$ — also known as β - n emitters — are the most important for reactor neutrino detectors as they can mimic an IBD event. The prompt signal is dominated by the kinetic energy of the β -electron, with contributions from all the daughters produced along to the decay path. Indistinguishable from that of an IBD, the delayed signal is provided by the neutron capture following the prompt. A veto rejecting all events following each muon cannot be applied without shrinking the live time to zero. This is due to a combination of the long lifetimes (257 ms for ${}^9\text{Li}$ and 172 ms for ${}^8\text{He}$) and the high muon rate at low overburdens. The difficulty of determining their contribution makes this cosmogenic background one of the most important to the measurement of θ_{13} and other liquid scintillator based experiments searching for IBDs, e.g

the upcoming JUNO experiment [5]. In DC, the difficulty has since been reduced by fitting the prompt energy spectrum simultaneously with θ_{13} instead of the distribution of time differences between cosmogenic decays and previous muons.

The Near (ND) and Far (FD) Detectors are protected by distinct overburdens of ~ 120 m.w.e (metre water equivalent) and ~ 300 m.w.e respectively. The profile of the overburdens means that each detector is subject to different muon fluxes and therefore cosmogenic background rates. Such backgrounds are partially rejected in the θ_{13} analysis by means of a veto relying on the following two characteristics: *i*) the β vertex should occur close to the reconstructed track of a preceding muon responsible for the spallation processes *ii*) multiple neutrons are often emitted in the spallation processes leading to multiple n -capture events occurring within 1 ms after the muon candidate, well before any significant fraction of the β - n emitters have started to decay.

The goal of this paper is the measurement of the ${}^9\text{Li}$ and ${}^8\text{He}$ production yields at the two detector sites (i.e. at different overburdens and therefore different mean muon energies). This begins with the generation of the expected ${}^9\text{Li}$ and ${}^8\text{He}$ spectra, described in section 3. Data selection, which ultimately contains a mixture of ${}^9\text{Li}$ and ${}^8\text{He}$ events is explained in section 4.1 and estimation of the ND and FD ${}^8\text{He}$ fractions are shown in section 4.2. The ${}^8\text{He}$ fraction is used in section 4.3 to estimate the yields and production rates of each cosmogenic radioisotope at the ND and FD. As the overburdens of the DC detectors are relatively shallow, especially for the ND which started taking data after the FD, they can be combined with existing measurements by KamLAND [6] and Borexino [7] to evaluate the exponential law [8] describing the production yield as a function of the mean muon energy. This relationship will allow future liquid scintillator experiments searching for IBD signals the capability to estimate their cosmogenic background rates.

2 The Double Chooz detectors

The ND and FD are almost identical in construction, but situated at ~ 400 m and ~ 1050 m from the Chooz Nuclear Power Plant reactors respectively. They are made of four concentric cylindrical vessels, of which, the innermost, the Neutrino Target (NT) is filled with 10.3 m^3 of Gd-loaded (0.1 wt.%) liquid scintillator. The NT is surrounded by 22.5 m^3 of Gd-free liquid scintillator called the Gamma Catcher (GC). The NT and GC vessels are made of transparent acrylic and together they form the fiducial volume used for the detection of IBDs and the cosmogenic β - n emitters. Gd has a larger cross section for neutron capture than H, so the majority of neutrons in the IBDs in the NT are captured on Gd, whilst in the GC there is no Gd so all the captures are on H. With its Gd-loading, the NT was meant to act as the detection volume for antineutrinos, but with novel background reduction techniques [2] the fiducial volume could be widened to include the GC. The liquid scintillator in the NT is composed of ortho-phenylxylylethane (o-PXE)/n-dodecane mixed in a volume ratio of 20/80, giving a ${}^{12}\text{C}$ density of $4.31 \times 10^{28}\text{ t}^{-1}$. The GC contains 66% mineral oil, 30% of n-dodecane and 4% o-PXE, giving a ${}^{12}\text{C}$ density of $4.29 \times 10^{28}\text{ t}^{-1}$.

The buffer encompasses the GC and is filled with non-scintillating mineral oil, acting as a shield from the surrounding radioactivity. Detection of the scintillation light is made

using 390 photomultiplier tubes (PMTs) housed within the buffer and attached to the surrounding stainless steel tank. These three inner regions are collectively called the Inner Detector (ID), outside of which is the Inner Veto (IV), filled with liquid scintillator and 78 PMTs used to detect cosmic muons and as a shield to external radiation. The ID and IV are then surrounded by another shield composed of 1 m of water in the ND and 15 cm of steel in the FD. Finally, the top of the detector is covered by plastic scintillator strips called the Outer muon Veto (OV). A detailed description of the detector is given in [1, 9].

3 Cosmogenic spectra prediction

The expected spectra of the ${}^9\text{Li}$ and ${}^8\text{He}$ decays are required to estimate their relative proportions and therefore rates produced in each detector. As the decay schemes are intricate, the standard GEANT4 [10–12] simulation toolkit cannot generate these spectra or provide a treatment of systematic uncertainties. Instead, each decay branch is simulated individually, the raw outgoing energies are fed into the GEANT4-based detector simulation and dynamically combined during error estimation.

3.1 Raw spectra generation

The decays of the cosmogenic radioisotopes ${}^9\text{Li}$ and ${}^8\text{He}$ release various particles which all appear at the same space–time point in the liquid scintillator. Such a property stems from the large widths of all the intermediate states in the decay trees, which go hand in hand with extremely short life–times. The instant observation of all these particles by the detector defines a single *prompt* event. For most decays, the energy signature of this prompt signal is dominated by the primary β –decay as contributions from heavier particles are quenched in the liquid scintillator.

After having thermalised, the neutron makes for a *delayed* event in which gammas from its capture are released into the scintillator. The energy spectrum of the delayed events provides no handle on the β – n emitter, so for the remainder of the paper *prompt energy spectrum* is referred to as *spectrum* for simplicity.

Figure 1 shows the decay schemes used in the simulation chain, ${}^9\text{Li}$ (left) and ${}^8\text{He}$ (right) where the mean value of the energy levels and the β –branching ratios are based on [13]. To correctly assess the energy deposited by each cosmogenic decay, predictions need to be made about the energies of all particles in the chain. In this work, the raw energies of the electrons, are computed using corrections to the Fermi theory for allowed β –decays. These corrections account for weak magnetism, radiative and finite–size effects. All the other particles, namely alphas, neutrons, gammas and tritons, are modelled using fully relativistic kinematics, correctly treating the recoil of light nuclei such as ${}^5\text{He}$. In the case of many–body break–ups, a recurrence method on the phase space — largely inspired by [14] — is implemented. The largeness of the state widths in the cosmogenic decay trees induces a bias on the mean energy of the states if they are generated following Lorentz distributions, as is custom with narrower widths. Instead, the decay chains have been modelled using Gaussian distributions.

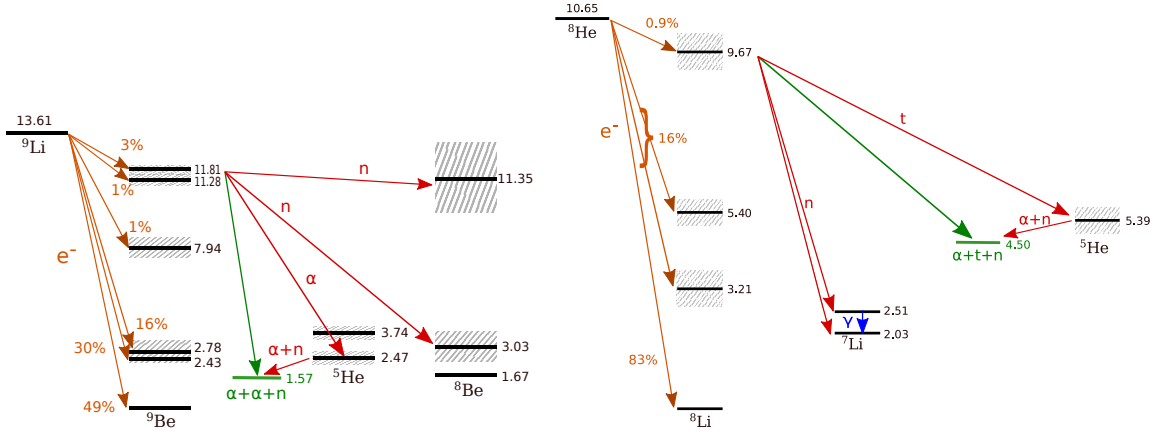


Figure 1. The decay schemes for ${}^9\text{Li}$ (left) and ${}^8\text{He}$ (right), where the energy widths of the states are proportional to the hatched boxes. The β -decay branching ratios are indicated along with some of the possible decay paths. The arrows indicate the particles released when a transition is made between levels. In both cases the energy levels are in MeV. For ${}^9\text{Li}$, the energy levels are quoted in relation to the ${}^9\text{Be}$ ground state and the final state for the β - n decay path is always $\alpha + \alpha + n$. For ${}^8\text{He}$, the energy levels are in relation to the ${}^8\text{Li}$ ground state. Note that the ground state of ${}^7\text{Li}$ is stable.

As there is little information about the decays following the primary β -decay in either decay tree, one raw spectrum is produced per branch in the tree. In total, this amounts to nine spectra for ${}^8\text{He}$, and twenty-four for ${}^9\text{Li}$, all under the form of HEP GEANT-compatible files. The position of the events in the ID are generated according to the ${}^{12}\text{C}$ density, whose value drives the cosmogenic isotope production.

These generated, raw events are then processed through the detector simulation as described in [1].

3.2 Mean spectrum and covariance building

The generation method presented in 3.1 has to be coupled with an error estimation tool to build a mean detected spectrum for each radioisotope.

The uncertainties on the branching ratios are included by varying their values between their physical bounds. When no nuclear data are available, this is achieved by uniformly selecting numbers at random so that the decay probabilities of one state add up to one. In the case of the branching ratios for the β -decays, or the strong decays of the 11.81 MeV level in ${}^9\text{Be}$, more constraining bounds — retrieved from published fits to experimental data [13, 15] — are utilised. Every set of the branching ratios thus picked produces a possible spectrum for the considered radioisotope. Such a spectrum is a realisation of the multivariate random variable \mathbf{B} , where \mathbf{B} stands for the vector of bin contents of the resulting spectrum. A $(n + 1)$ -th realisation $\mathbf{b}^{(n+1)}$ of the random variable \mathbf{B} , updates the estimator \hat{V} of the covariance matrix between the different bin contents as follows:

$$\hat{V}_{n+1} = \frac{1}{n} \sum_{k=1}^{n+1} \left(\mathbf{b}^{(k)} - \bar{\mathbf{b}}_{n+1} \right) \left(\mathbf{b}^{(k)} - \bar{\mathbf{b}}_{n+1} \right)^T, \quad (3.1)$$

where $\bar{\mathbf{b}}_{n+1}$ is the sample mean. The size of \hat{V} is the square of the number of energy bins. Convergence is assumed after a few million iterations when the last fifty matrices are close to one another.

A second matrix W , which represents the systematic uncertainty on the weak magnetism correction, is added to \hat{V} . This matrix reads $W = \boldsymbol{\sigma}\boldsymbol{\sigma}^T$ with $\boldsymbol{\sigma}$ the vector of errors defined by $\sigma_i = Ce_iB_i$, where C is the slope of the error, e_i the i -th bin centre of the histogram representing the spectrum, and B_i the content of the i -th bin. The value of C was set to $C = 0.005 \text{ MeV}^{-1}$. This represents a conservative 100% error on the value of the weak magnetism correction for allowed transitions (when compared to the linearisation of the correction found in [16]). It should be noted that the relative importance of this uncertainty increases with energy, as does the contribution of the electrons to the bin contents of the resulting spectrum.

Separate predicted spectra are created depending on whether the neutron is captured on Gd or H. This is because the energy scale is treated differently for each as they dominate different volumes of the detector, with slightly separate properties. As a result the correlations between the predicted spectra had to be derived. For each cosmogenic radioisotope, the covariance between the predicted spectra S^{Gd} (obtained from an analysis of the raw spectra on Gd) and S^{H} (from an analysis on H), has been computed using a variation of the aforementioned technique. Regardless of the capture used, the ${}^9\text{Li}$ and ${}^8\text{He}$ spectra are not correlated.

3.3 Resulting ${}^9\text{Li}$ and ${}^8\text{He}$ spectra

The predicted spectra from the error estimator described in section 3.2 are used as inputs in the fit to the data in section 4.2. For each radioisotope, and for each neutron capture type, the prediction comes from the sample mean $\bar{\mathbf{b}}$ for the iteration when convergence was reached. The predicted spectra which are relevant when combining the Gd and H data sets are plotted in figure 2.

In the case of ${}^9\text{Li}$, the low energy region (at around 2 MeV) has non-negligible contributions from the strong decays of the levels above the one at 2.78 MeV in ${}^9\text{Be}$. The ratios for these decays are little constrained, hence the sizeable uncertainty in that area. Above 4 MeV, electrons start dominating the energy depositions, and the weak magnetism uncertainty takes over as the β ratios are well-known. Since ${}^8\text{He}$ has a lower endpoint than ${}^9\text{Li}$, the uncertainty on the β branching ratios dominates compared to the weak magnetism uncertainty. Unfortunately, the β ratios feeding the two most populated β - n states in ${}^8\text{Li}$ had to be extracted from approximate fits [17].

4 Measurements

The selection of a highly pure sample of β - n emitters is explained in the first part of this section. This sample of events contains a mixture of the cosmogenically produced ${}^9\text{Li}$ and ${}^8\text{He}$ decays, in unknown quantities. The second part describes how the predicted spectra are used to separate a background subtracted, and therefore pure sample of β - n emitters into their constituent quantities, denoted by the ${}^8\text{He}$ fraction for the ND and FD. The third

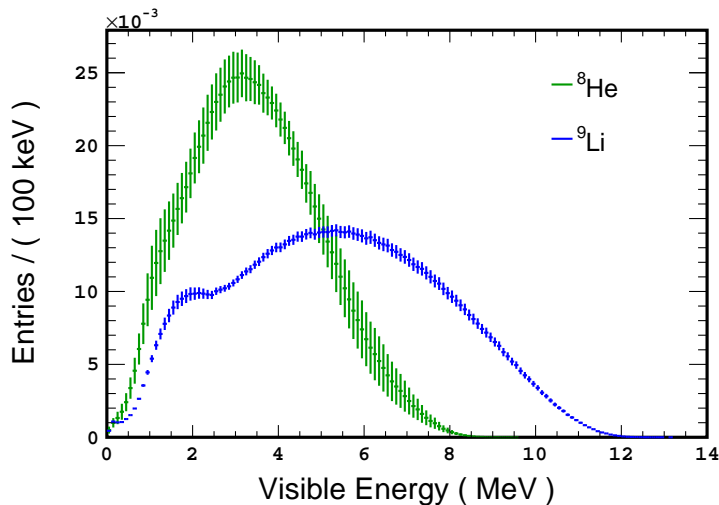


Figure 2. Mean simulated ${}^8\text{He}$ and ${}^9\text{Li}$ spectra. The simulated spectra shown correspond to decays where the emitted neutron’s capture has been observed on H or Gd. Each spectrum is normalised to unity. The errors come from the covariance matrices associated with these spectra.

part uses the ${}^8\text{He}$ fractions to estimate the total number of ${}^9\text{Li}$ and ${}^8\text{He}$ produced in each detector from the total measured β - n rates. The ${}^9\text{Li}$ yields are finally compared to other liquid scintillator experiments who have made similar measurements.

4.1 Selection of ${}^9\text{Li}$ and ${}^8\text{He}$ Candidates

Preliminary selection follows the same criteria as for IBDs published in [1] and [2], corresponding to delayed neutron capture on Gd and H respectively. These selections are united to combine the GC and NT volumes used in the analysis. Prompt candidate selection fell within the visible energy range $0.5 \leq E_p < 20 \text{ MeV}$ and the delayed neutron within $1.3 \leq E_d < 10 \text{ MeV}$. An artificial neural network trained on simulated IBD events, used three variables: *i*) the time and *ii*) distance between prompt and delayed events and *iii*) the delayed visible energy to further reduce backgrounds. These selection criteria identify coincident signals composed mainly of IBD candidates which are used to measure the neutrino mixing angle θ_{13} . However, part of the cosmogenic background can be separated by means of a posterior probability P . These events removed from the IBD candidates form a relatively pure sample of ${}^9\text{Li}$ and ${}^8\text{He}$ events which can be used to estimate the ${}^8\text{He}$ fraction in section 4.2.

The probability $P(\text{cos} | n, d)$ for a prompt candidate to represent a cosmogenic decay, given that there exists a muon at a distance d from it, which produced n neutrons within 1 ms, is defined by Bayes’ theorem:

$$P(\text{cos} | n, d) = \frac{\pi_r f_{\text{cos}}(n, d)}{\pi_r f_{\text{cos}}(n, d) + f_{\text{acc}}(n, d)}. \quad (4.1)$$

where f_{cos} denotes the joint probability density of n and d for cosmogenics and f_{acc} represents accidental coincidences between IBD candidates and muons. Including variables other

than d and n did not improve the selection efficiency of cosmogenic decays. The prior ratio π_r is defined as the ratio of the expected cosmogenic rate r_{cos} to the product of the IBD candidate rate r_{cand} , the muon rate r_μ and the length $t_{\mathcal{W}}$ of the time window \mathcal{W} used for coincidences:

$$\pi_r = \frac{r_{cos}}{r_{cand} r_\mu t_{\mathcal{W}}} . \quad (4.2)$$

For $t_{\mathcal{W}} = 700$ ms, the prior ratios evaluate to 7.7×10^{-3} and 5.5×10^{-4} , at FD and ND respectively. It is worth stressing that the cosmogenic selection at the ND is all the more difficult that the IBD rate is higher there than at the FD. On the other hand, the increase in the muon rate is largely absorbed by the increase in r_{cos} .

The scarcity of ${}^9\text{Li}$ and ${}^8\text{He}$ events makes them difficult to use to create f_{cos} . Instead, another radioactive isotope ${}^{12}\text{B}$, produced by muons in larger abundance, is utilised. Although the real distribution of cosmogenic radioisotope production relative to the muon is wider for ${}^{12}\text{B}$, position reconstruction and geometrical effects of the relatively small detector mean that the observed probability densities are similar. The so-called on-time window, for the identification of ${}^{12}\text{B}$ correlated events, is shifted by 1 ms from muons prior to a prompt candidate; this removes cosmic neutrons, whose capture time is much smaller than the lifetime of the β - n emitters. The distribution of the accidental background is determined using several off-time windows which are shifted by more than 10 s. Subtracting the average of these from the on-time window they provide f_{cos} , normalised to unity they provide f_{acc} . The distributions thus obtained were cross-checked against that of ${}^9\text{Li}+{}^8\text{He}$ and found to agree within the statistical uncertainty.

The posterior probability from (4.1) is calculated for each prompt candidate p and all the muons μ in the window \mathcal{W}_p preceding each p . In the θ_{13} analysis [1, 2], the aim was to veto cosmogenic events, dominated by β - n emitters but including to a lesser degree others such as ${}^{12}\text{B}$. This was achieved by calculating a single (cosmogenic) probability for each prompt by selecting the maximum value as follows:

$$P_{max}(cos) = \max_{\mu \in \mathcal{W}_p} P(cos | n_\mu, d_{p-\mu}) . \quad (4.3)$$

If $P_{max}(cos) > 0.4$, the prompt event was vetoed as a ${}^9\text{Li}$ or ${}^8\text{He}$ candidate and used in section 4.2.

4.2 ${}^8\text{He}$ Fraction Measurements

The events selected by $P_{max}(cos) > 0.4$ in section 4.1 are used to create the data spectra. They take advantage of two available variables, time to the previous muon T and prompt visible energy E_p . The accidental component is estimated using muon-prompt pairs between 2–20 s before the prompt event and then subtracted to give a pure sample of ${}^9\text{Li}$ and ${}^8\text{He}$ events. Two-component χ^2 fits of the data spectra are performed where the two free parameters are the number of ${}^9\text{Li}$ events n^{Li} and the number of ${}^8\text{He}$ events n^{He} . The results are quoted in terms of the fraction of ${}^8\text{He}$ events $f^{\text{He}} = n^{\text{He}}/(n^{\text{He}} + n^{\text{Li}})$ and are corrected for time and visible energy cuts. The fit is performed separately for the ND and FD as differing overburdens suggest that their ${}^8\text{He}$ fractions may not be the same.

A bin size of 1 MeV was used along the energy axis within the range $0.5 < E_p < 10.5$ MeV and two bins were used along the time axis, the first 100 ms and the second 600 ms long. The fitting procedure was tested using fake data to choose a bin size which did not bias the results because of the limited statistics and the Gaussian nature of the χ^2 approach.

The χ^2 is constructed as follows:

$$\chi^2 = \mathbf{y}^T \left(\mathbf{M}_{stat} + \sum_j \sum_c^{\text{H,Gd } ^9\text{Li, } ^8\text{He}} \mathbf{M}_{spec}^{c,j} \right)^{-1} \mathbf{y}, \quad (4.4)$$

where \mathbf{M}_{stat} is the covariance matrix corresponding to the statistical uncertainty and $\mathbf{M}_{spec} = \hat{V} + W$ is the covariance matrix corresponding to the branching ratio and weak magnetism uncertainty from section 3.2. $\mathbf{y} = y_{(t,e)} - \mu_{(t,e)}$ is the difference between the data and expected value for each bin, where e corresponds to the bin number along the energy axis and t along the time axis. The expected value for each bin is evaluated as follows:

$$\mu_{(t,e)} = \sum_j \sum_c^{\text{H,Gd } ^9\text{Li, } ^8\text{He}} F_j n^c \left(e^{-\frac{T_t}{\tau_c}} - e^{-\frac{T_{t+1}}{\tau_c}} \right) S(E_p)_e^{c,j}, \quad (4.5)$$

where F_j is the fraction of events where the neutron was captured on H or Gd, c is the cosmogenic radioisotope ^9Li or ^8He , τ_c is the lifetime 257 ms for ^9Li and 172 ms for ^8He , T_t is the start of the time bin t and $S(E_p)_e^{c,j}$ is the fraction of the predicted spectrum expected in bin e . The effect of the energy scale uncertainty on the fit results was tested by altering the spectra by $\pm 1\sigma$ uncertainty. It was found to be negligible as a result of the much larger statistical uncertainty.

For the ND, $f_{ND}^{He} = (-1.5 \pm 4.5)\%$ with $\chi^2/d.o.f = 16.5/18$ giving a probability $p = 0.56$. For the FD, $f_{FD}^{He} = (2.9 \pm 3.5)\%$ with $\chi^2/d.o.f = 33.5/18$ giving $p = 0.01$. Both results return a ^8He component compatible with zero. The fit results can be seen as a function of E_{vis} , summed along the time axis in figure 3 for the ND (left) and FD (right). The pink error bands represent the uncertainty on the predicted spectrum.

4.3 Cosmogenic yields, production rates and cross sections

Constraints on the ^8He fractions from the previous section allow the ^9Li and ^8He yields, production rates and cross sections to be quoted separately. Furthermore, as the overburdens are different at the ND and FD sites the dependence of production yield on $\langle E_\mu \rangle$ can be investigated. The results can then be compared to measurements of β - n emitters from other experiments with different overburdens, such as KamLAND and Borexino. This means the energy dependence of the production yield can be constrained and their rates can be predicted at the sites of future liquid scintillator experiments.

Each detector's livetime, measured β - n rates and their efficiencies are summarised in Table 1. The β - n rates $r_{\beta-n}$ are measured for the energy range $1.0 < E_p < 20$ MeV. They are separated into two categories, selected using equation 4.3 and correspond to $P_{max} > 0.4$ and $P_{max} < 0.4$. The latter is dominated by IBDs making a measurement of the β - n

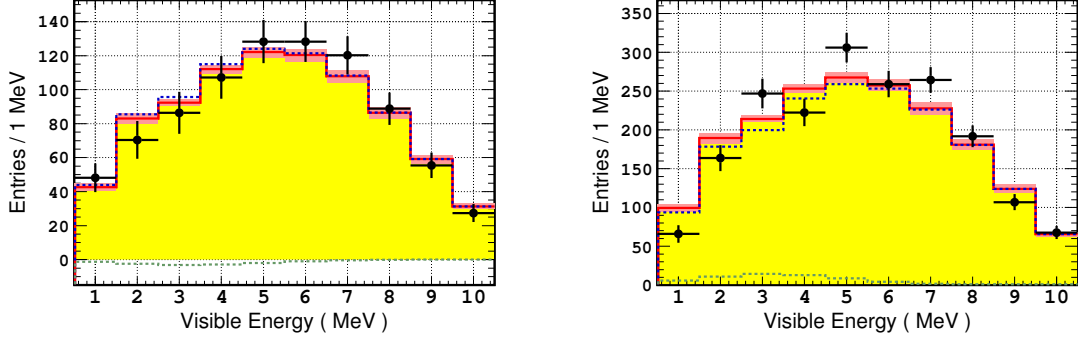


Figure 3. The ND (left) and FD (right) visible energy spectra of the ${}^9\text{Li}+{}^8\text{He}$ data (black points). Overlain are the best fit results with ${}^9\text{Li}$ (blue dashed line), ${}^8\text{He}$ (green dashed line) and their sum (solid red line). The pink error bands represent the uncertainty on the predicted spectrum. The goodness of the fits are $\chi^2/d.o.f = 16.5/18$ (ND) and $\chi^2/d.o.f = 33.5/18$ (FD).

	ND	FD
livetime (days)	257.96	825.34
$\epsilon_{\beta-n}$ (%)	81.7 ± 0.1	84.2 ± 2.0
$r_{\beta-n}$ (day^{-1})	$P_{max} < 0.4$	14.71 ± 1.50
	$P_{max} > 0.4$	2.68 ± 0.28
	Total	3.99 ± 0.14
	18.7 ± 1.51	5.46 ± 0.29

Table 1. The livetime, β - n rates and their efficiencies $\epsilon_{\beta-n}$ used to estimate the yields, production rates and cross sections.

emitters to a reasonable level of accuracy challenging. Their rates are evaluated with a fit to the prompt energy which includes IBDs and further backgrounds; they are given in Table 1. They are cross-checked using a fit to the distribution of time differences between the prompt event and previous muons giving $12.32 \pm 2.01 \text{ day}^{-1}$ and $3.01 \pm 0.60 \text{ day}^{-1}$ for the ND and FD respectively. The β - n rates for $P_{max} > 0.4$ are also measured using the time distribution to previous muons and are added to those for $P_{max} < 0.4$ to give the total, also shown in Table 1. The ${}^8\text{He}$ fraction measurements from section 4.2 are used to estimate the corresponding rates r_c of each cosmogenic radioisotope c by splitting the total β - n rates into their respective ${}^8\text{He}$ and ${}^9\text{Li}$ components after which they are further corrected for cosmogenic dependent efficiencies. The ${}^8\text{He}$ fraction measurements are assumed to be the same for both $P_{max} < 0.4$ and $P_{max} > 0.4$.

The yield is defined in [6, 7] as follows:

$$Y_c = \frac{\mathcal{N}_c}{R_\mu T_L \cdot \langle L_\mu \rangle \cdot \rho}, \quad (4.6)$$

and the production rate as:

$$R_c = \frac{\mathcal{N}_c}{V \cdot \rho \cdot T_L}, \quad (4.7)$$

	c	$Y (\times 10^{-8} \mu^{-1} \text{g}^{-1} \text{cm}^2)$	$R (\text{kton}^{-1} \text{d}^{-1})$	$\sigma (\mu \text{barns})$
ND	${}^9\text{Li}$	4.37 ± 0.49	1375 ± 154	0.87 ± 0.10
	${}^8\text{He}$	< 4.74	< 1492	< 0.95
FD	${}^9\text{Li}$	7.98 ± 0.52	483 ± 32	1.59 ± 0.10
	${}^8\text{He}$	0.39 ± 1.16	24 ± 70	0.08 ± 0.23

Table 2. The yields Y , production rates R and cross sections for ${}^9\text{Li}$ and ${}^8\text{He}$ produced in the ND and FD. In the ND case the ${}^9\text{Li}$ values are calculated for $f^{He} = 0\%$ and a 3σ upper limit is given for the ${}^8\text{He}$ values.

where $\mathcal{N}_c = (r_c \cdot T_L)/\epsilon_c$ is the total number of the cosmogenic radioisotope c created in the total liquid scintillator volume $V = 32.8 \text{ m}^3$, ϵ_c is the product of all efficiencies, e.g detection and non β -n branching ratios (49% for ${}^9\text{Li}$ and 84% for ${}^8\text{He}$), R_μ is the muon rate in V , $\langle L_\mu \rangle$ is the average muon track length in the volume, T_L is the live time, the density $\rho = 0.8 \text{ g cm}^{-3}$ and r_c is the total β -n rate, separated using the ${}^8\text{He}$ fraction measured in section 4.2. As the muon flux can be defined as $\phi_\mu = R_\mu \langle L_\mu \rangle / V$ a substitution can be made into equation 4.6 to give a new definition of the yield as:

$$Y_c = \frac{\mathcal{N}_c}{\phi_\mu \cdot V \cdot T_L \cdot \rho}, \quad (4.8)$$

where the muon fluxes are $3.64 \pm 0.04 \text{ m}^{-2} \text{ s}^{-1}$ and $0.70 \pm 0.01 \text{ m}^{-2} \text{ s}^{-1}$ for the ND and FD respectively, measured using data in [18]. The production cross section can be inferred from the yield via the relation:

$$Y_c = \frac{\sigma_c}{m_T}, \quad (4.9)$$

where m_T is the mass of the target atom, in this case ${}^{12}\text{C}$. It should be noted that this cross section is averaged over the muon energy spectrum corresponding to the specific detector depth. The yields, production rates and cross sections for the ND and FD are given in Table 2.

As discussed in [8], the yields follow a dependence on the mean muon energy E_μ according to a power exponent α as $Y \propto E_\mu^\alpha$. In the case of underground sites the yield is given as a function of the mean muon energy which can be fitted with:

$$Y = Y_0 \langle E_\mu \rangle^{\bar{\alpha}}, \quad (4.10)$$

where $\bar{\alpha}$ is used to denote the power law as a function of $\langle E_\mu \rangle$ instead of a mono-energetic muon energy. The mean muon energies at the ND and FD are $32.1 \pm 2.0 \text{ GeV}$ and $63.7 \pm 5.5 \text{ GeV}$ respectively, evaluated with a dedicated MUSIC simulation [19]. The yields can be compared to measurements by KamLAND [6], Borexino [7] and Daya Bay [20, 21] as demonstrated in figure 4, where the values have been corrected to represent the carbon density of the DC detectors. The Daya Bay yields are estimated from their β -n rates at each experimental hall assuming they contain 100% ${}^9\text{Li}$. As such, and because not all of the uncertainties and efficiencies are known, they are omitted from the fit for $\bar{\alpha}$. Also included

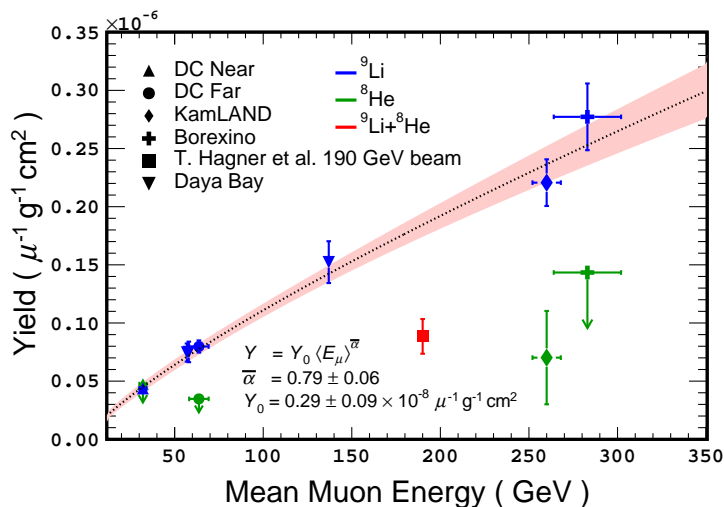


Figure 4. The ND and FD yields shown separately for ${}^9\text{Li}$ and ${}^8\text{He}$ as a function of the mean muon energy $\langle E_\mu \rangle$, alongside those from KamLAND, Borexino and Daya Bay. The arrows depict a 3σ upper limit and their lengths equal 1σ . A fit to the ${}^9\text{Li}$ yields of the ND, FD, Borexino and KamLAND returns the power law exponent $\bar{\alpha} = 0.79 \pm 0.06$ with $\chi^2/d.o.f = 2.4/2$.

in the figure is a measurement at CERN using the SPS muon beam aimed at a liquid scintillator target, where the combined cross section for ${}^9\text{Li}+{}^8\text{He}$ is shown converted into the yield using equation 4.9 and corrected by a factor of 0.87 ± 0.03 to take into account the energy spectrum of cosmic muons [8]. This measurement underestimates the expected yield in figure 4, and is confirmed for other radioisotopes where their predicted rates for ${}^{11}\text{C}$, ${}^8\text{Li}$, ${}^8\text{B}$ and ${}^6\text{He}$ are lower than subsequent measurements by Borexino [7]. This could be due to an underestimation of the efficiency used to correct for the radioisotope production at larger distances from the muon beam.

A covariance matrix, separating the uncertainties on the yields and mean muon energies between the ND and FD into their correlated and uncorrelated parts, is used when performing the fit to the ${}^9\text{Li}$ yields, giving $\bar{\alpha} = 0.79 \pm 0.06$ and $Y_0 = (0.29 \pm 0.09) \times 10^{-8} \mu^{-1} \text{g}^{-1} \text{cm}^2$ with a correlation of $\rho = -0.98$. The minimum was found at $\chi^2/d.o.f = 2.4/2$, demonstrating the reliability of the model over these detector depths. No such fit was performed for ${}^8\text{He}$ as the values are compatible with zero.

5 Conclusion

The long-lived β - n emitters produced in the Double Chooz ND and FD by spallation interactions of high-energy muons satisfy the time and energy selection criteria of IBD candidates. The distance between the muon track and prompt signal of the IBD along with the neutron multiplicity following that muon can be used to effectively select a pure sample of cosmogenic events.

The two components expected to form the selected β - n emitters of the ND and FD are ${}^9\text{Li}$ and to a smaller extent ${}^8\text{He}$. Thanks to accurate simulations of the complex decays

schemes of these radioisotopes and the following detector response to the complete set of final states, a fit of these two components could be performed. A strong constraint has been set on the production rate of the ^8He radioisotope, found to be compatible with zero at both detector sites.

A clear relationship between the production yield of the ^9Li radioisotope with $\langle E_\mu \rangle$ has been measured between the two detector sites attributed to the different muon spectra reaching the fiducial volume ($32.1 \pm 2.0 \text{ GeV}$ for the ND and $63.7 \pm 5.5 \text{ GeV}$ for the FD). These results extend the study of ^9Li production towards smaller mean muon energies than other published experiments. Combining all available data a simple power law (equation 4.10) is found to describe the ^9Li production yield with good accuracy over one order of magnitude in the muon energy and does not match the independent measurement performed with a 190 MeV monochromatic muon beam. This power law provides a new reference for future liquid scintillator based reactor neutrino experiments, e.g JUNO, for which an estimate of their cosmogenic background is highly relevant. Given a mean muon energy of 215 GeV, the ^9Li yield for JUNO is estimated to be $(2.03 \pm 0.12) \times 10^{-7} \mu^{-1} \text{g}^{-1} \text{cm}^2$. It should be noted that this does not include the uncertainty on JUNO's mean muon energy.

Acknowledgments

We thank the French electricity company EDF; the European fund FEDER; the Région de Champagne Ardenne; the Département des Ardennes; and the Communauté de Communes Ardenne Rives de Meuse. We acknowledge the support of the CEA, CNRS/IN2P3, the computer centre CC-IN2P3 and LabEx UnivEarthS in France; the Max Planck Gesellschaft, the Deutsche Forschungsgemeinschaft DFG, the Transregional Collaborative Research Center TR27, the excellence cluster “Origin and Structure of the Universe” and the Maier-Leibnitz-Laboratorium Garching in Germany; the Ministry of Education, Culture, Sports, Science and Technology of Japan (MEXT) and the Japan Society for the Promotion of Science (JSPS) in Japan; the Ministerio de Economía, Industria y Competitividad (SEIDI-MINECO) under grants FPA2016-77347-C2-1-P and MDM-2015-0509 in Spain; the Department of Energy and the National Science Foundation and Department of Energy in the United States; the Russian Academy of Science, the Kurchatov Institute and the Russian Foundation for Basic Research (RFBR) in Russia; the Brazilian Ministry of Science, Technology and Innovation (MCTI), the Financiadora de Estudos e Projetos (FINEP), the Conselho Nacional de Desenvolvimento Científico e Tecnológico (CNPq), the São Paulo Research Foundation (FAPESP) and the Brazilian Network for High Energy Physics (RENAFAE) in Brazil.

References

- [1] Y. Abe et al., *Improved measurements of the neutrino mixing angle θ_{13} with the Double Chooz detector* *JHEP* (2014) 086.
- [2] Y. Abe et al., *Measurement of θ_{13} in Double Chooz using neutron captures on hydrogen with novel background rejection techniques* *JHEP* (2016) 163.

- [3] Double Chooz Collaboration, Anatael Cabrera *Double Chooz Improved Multi-Detector Measurements* EP Seminar/Colloquium at CERN, Sept. 2016.
- [4] Abe, Y. et al., *Muon capture on light isotopes measured with the Double Chooz detector* *Phys. Rev. C* **93** (2016) 054608.
- [5] F. An et al., *Neutrino Physics with JUNO* *J. Phys. G* **43** (2016) 030401.
- [6] S. Abe et al., *Production of Radioactive Isotopes through Cosmic Muon Spallation in KamLAND* *Phys. Rev. C* **81** (2010) 025807.
- [7] G. Bellini et al., *Cosmogenic Backgrounds in Borexino at 3800 m water-equivalent depth* *JCAP* (2013) 049.
- [8] T. Hagner et al., *Muon-induced production of radioactive isotopes in scintillation detectors* *Astroparticle Physics* **14** (2000) 33-47.
- [9] Y. Abe et al., *Phys. Reactor $\bar{\nu}_e$ disappearance in the Double Chooz experiment* *Phys. Rev. D* **86** (2012) 052008.
- [10] J. Allison et al., *Recent Developments in Geant4* *Nucl. Instrum. Meth. A* **835** (2016) 186-225.
- [11] J. Allison et al., *Geant4 Developments and Applications* *IEEE Transactions on Nuclear Science* **53** No. 1 (2006) 270-278.
- [12] S. Agostinelli et al., *Geant4 - A Simulation Toolkit* *Nucl. Instrum. Meth. A* **506** (2003) 250-303.
- [13] D.R. Tilley et al., *Energy levels of light nuclei $A = 8,9,10$* *Nucl. Phys. A* **745** (2004) 155-362.
- [14] R. Hagedorn *Relativistic Kinematics: A Guide to the Kinematic Problems of High-Energy Physics* W. A. Benjamin (1963).
- [15] Y. Prezado et al., *Large asymmetry in the strongest β -transition for $A=9$* *Phys. Lett. B* **576** (2003) 55-61.
- [16] A.C. Hayes et al., *Systematic Uncertainties in the Analysis of the Reactor Neutrino Anomaly* *Phys. Rev. Lett.* **112** (2014) 202501.
- [17] F.C. Barker and E.K. Warburton, *The beta-decay of ^8He* *Nucl. Phys. A* **487** (1988) 269-278.
- [18] T. Abrahão et al., *Cosmic-muon characterization and annual modulation measurement with Double Chooz detectors* *JCAP* (2017) 017.
- [19] P. Antonioli et al., *A three-dimensional code for muon propagation through the rock: MUSIC* *Astroparticle Physics* **7** (1997) 357.
- [20] F. P. An et al., *Measurement of electron antineutrino oscillation based on 1230 days of operation of the Daya Bay experiment* *Phys. Rev. D* **95** (2017) 072006.
- [21] F. P. An et al., *The muon system of the Daya Bay Reactor antineutrino experiment* *Nucl. Instrum. Meth. A* **773** (2015) 8-20.